CARBON 68 (2014) 734–741

Available at www.sciencedirect.com

ScienceDirect

journal homepage: www.elsevier.com/locate/carbon

Tailoring the performance of graphene-based supercapacitors using topological defects: A theoretical assessment

Alexander J. Pak, Eunsu Paek, Gyeong S. Hwang *

Department of Chemical Engineering, University of Texas, Austin, TX 78712, USA

ARTICLE INFO

Article history:
Received 22 September 2013
Accepted 22 November 2013
Available online 1 December 2013

ABSTRACT

Graphene-based materials have been proposed as promising electrodes for electric double layer capacitors. Recently, it has been found that one of the limitations of graphene electrodes is the finite quantum capacitance at low applied voltage. In this work, we investigate the impact of having point-like topological defects in graphene on the electronic structure and quantum capacitance. Our results clearly show that the presence of defects, such as Stone Wales, di-vacancies, and di-interstitials, can substantially enhance the quantum capacitance when compared to pristine graphene, which is found to be due to defect-induced quasi-localized states near the Fermi level. In addition, the charging behavior tends to be asymmetric around the neutrality point. We also discuss the possibility of tuning the electronic structure and capacitance through mixtures of these defects. Our findings suggest that graphene-based electrodes with topological defects may demonstrate noteworthy capacitance but should be carefully selected for use as either the positive or negative electrode.

1. Introduction

Supercapacitors, a class of electrochemical energy storage devices with high power densities and lifetimes [1], have become increasingly ubiquitous in our energy landscape. Yet their energy densities tend to be at least an order of magnitude less than conventional batteries, which has motivated research focused on improving the capacitance [2,3]. Graphene-based materials are attractive candidates as next-generation electrodes for supercapacitors due to their high theoretical specific surface area and electrical conductivity [4–8]. Despite these favorable qualities, practical implementation of these materials has been limited by poor volumetric surface area and/or accessibility to the electrolyte [9–16].

Several reports have demonstrated that doping or functionalization of graphene can enhance the capacitance considerably, which is suggested to be due to a combination of facilitated electrolyte wettability and electrode accessibility, increased electrical conductivity, and possible pseudocapacitance [17–20]. Recently, the electrode capacitance was also demonstrated to be an important factor; for example, the quantum capacitance of graphene has been found to limit performance at low applied potential [21–23]. In the case of nitrogen-doped graphene, the observed improvement in capacitance has been shown to be, in part, due to the enhanced quantum capacitance [24,25]. This can be particularly true when using ionic liquids (ILs), solvent-free electrolytes with large electrochemical windows, as their chemical stabilities may preclude pseudocapacitive behavior [26,27]. Since the quantum capacitance is proportional to the electronic density of states (DOS) [28], it is plausible that other dopants, functional groups, topological defects, adsorbates, and combinations thereof may also modify the electronic structure and thus, the capacitance. Among these, topological defects

* *Corresponding author:* Fax: +1 (512) 471 7060.
E-mail address: gshwang@che.utexas.edu (G.S. Hwang).
0008-6223/$ - see front matter
http://dx.doi.org/10.1016/j.carbon.2013.11.057

have been readily observed as a consequence of graphene growth conditions or processing by irradiation or chemical treatment [29–32].

In this paper, we examine the impact of topological defects on the electronic structure and quantum capacitance of graphene. To this end, we simulated graphene electrodes with individual point-like topological defects such as Stone Wales, di-vacancies, and di-interstitials at a defect density $n_d = 3 \times 10^{13}$ cm^{-2} (≈0.8 at.%) using density functional theory (DFT). Based on our results, we also discuss how these topological defects can be utilized to improve the overall performance of graphene-based supercapacitors.

2. Computational methods

The atomic and electronic structures of pristine and defective graphene sheets were calculated using DFT within the Perdew-Wang 91 generalized gradient approximation (GGA-PW91) [33], as implemented in the Vienna Ab-initio Simulation Package (VASP) [34]. We employed the projector augmented wave (PAW) method to describe the interaction between ion core and valence electrons [35], and a plane-wave basis set with a kinetic energy cutoff of 400 eV. We used a hexagonal 8×8 supercell with a GGA-optimized lattice constant of 2.466 Å and a vacuum space of 15 Å in the z direction to avoid interactions with the periodic image. Each supercell has one defect, corresponding to a defect density of 3.0×10^{13} cm^{-2} (≈0.8 at.%). For the Brillouin zone integration, we used a $(6 \times 6 \times 1)$ Monkhorst-Pack (M-P) [36] k-point mesh for geometry optimization and energy calculations and a $(12 \times 12 \times 1)$ M-P k-point mesh for electronic structure calculations. Bader charge [37] distributions were calculated using a rectangular 4×8 supercell with the same lattice constant, vacuum spacing, and k-point mesh when both charge neutral and with the injection of one electron or hole. The larger, mixed-defect system was created using a hexagonal 16×16 supercell with 15 Å of vacuum space; here, $(3 \times 3 \times 1)$ and $(6 \times 6 \times 1)$ M-P k-point meshes were used for geometry optimization and electronic structure calculations, respectively.

3. Results and discussion

A variety of topological defects can be found in graphene, including the three types of point-like defects considered here: Stone Wales (SW), di-vacancies (DVs), and di-interstitials (DIs). The most fundamental of these is the SW defect [38], which occurs when a C–C bond rotates in-plane 90° and results in the structure with two pentagons and two heptagons as shown in Fig. 1(a). According to our DFT-GGA calculations, the formation energy $E_f = 5.0$ eV, which is in good agreement with previously reported values (≈5 eV) [39,40].

DVs in graphene can be created through either the agglomeration of mono-vacancies or the ejection of adjacent C atoms and have been observed using high resolution transmission electron microscopy [30–32]. Fig. 1(b–d) shows three possible DV reconstructions: V_2(555-777), V_2(5555-6-7777), and V_2(5-8-5) [29,30]. The predicted E_f of these defects range from $6.7 < 7.2 < 7.6$ eV for V_2(555-777) < V_2(5555-6-7777) < V_2(5-8-5). DV defects also tend to be stationary with a migration barrier around 7 eV [41]. Mono-vacancies, on the other hand, tend to be mobile (with a barrier of 1–2 eV) [41] and can be annihilated after thermal annealing. We therefore do not consider mono-vacancies in this analysis.

The formation of DIs have been proposed through the adsorption of C–C dimers, which results in local corrugations or so-called hillocks [42,43]. Fig. 1(e–g) shows three minimum-energy DI structures considered: the inverse SW I_2(ISW), I_2(555-6-777), and I_2(5555-66-7777). The E_f of these defects are predicted to range from $6.2 < 6.6 < 7.3$ eV for I_2-(ISW) < I_2(555-6-777) < I_2(5555-66-7777). Similar to DVs, DI defects are also expected to be fairly stationary, although single C adatoms have been predicted to be mobile with a barrier of 0.4–0.9 eV [44,45].

3.1. Defect-induced modification of electronic structure

We calculated the electronic band structure and density of states (DOS) of each of the fully relaxed defects using DFT. Point-like topological defects locally reconstruct the lattice and thereby reduce the six-fold symmetry of graphene (D_{6h}) to either twofold (D_{2h} or C_{2v}) or threefold (D_{3h} or C_{3v}) symmetry. The high symmetry lines along the Γ-K-M-Γ Brillouin zone (BZ) path are usually sufficient to represent the important features of the band structure for six- and three-fold symmetry. However, the two K_1/K_2 and M_1/M_2 are no longer symmetric in the case of twofold symmetry [Fig. 2]. We therefore compare the extended Γ-K_1-M_1-Γ-M_2-K_2-Γ BZ path for each defect, despite the redundancy in the threefold cases.

Fig. 3 shows the band structure [left] and DOS [middle] of the SW defect (black) compared to pristine graphene (red, dashed). In the latter case, the valence (VB) and conduction (CB) bands display linear dispersion that extends about 1 eV. In the SW case, however, the bands near the Fermi level (E_F) are partially flattened; this effect is more marked around 0.45 and 0.60 eV above E_F and gives rise to the distinct peaks in the DOS that are a well-known characteristic of the SW defect [46,47]. These flat bands are indicative of the quasi-localization of the p_z states in the vicinity of the SW defect, due to the disruption of the graphene π system. Hence, injected charge carriers, especially electrons, will accumulate near the pentagon–heptagon C rings, as seen from the band decomposed charge density isosurfaces [right]. However, the flat bands are also smoothly connected to the low-energy dispersion of graphene (more so in the filled states), which suggests that a large fraction of the excess charge can also widely spread over the graphene lattice.

Fig. 4 shows the band structures [left] and DOS [middle] for each of the DV structures. In all three cases, the E_F is shifted down below the VB of graphene primarily due to electron deficiency; note that V_2 removes two electrons from the π system of graphene. The DOS plots show several pronounced peaks near the E_F which correspond to partial flattening of the bands, in good agreement with previous work [45,46]. This is apparently attributed to the quasi-localized p_z states in the vicinity of the DV defects, as also depicted in the band decomposed charge density isosurfaces. The degree of localization, however, tends to successively decrease in the V_2(555-777), V_2(5555-6-7777), and V_2(5-8-5) cases; this is well demonstrated

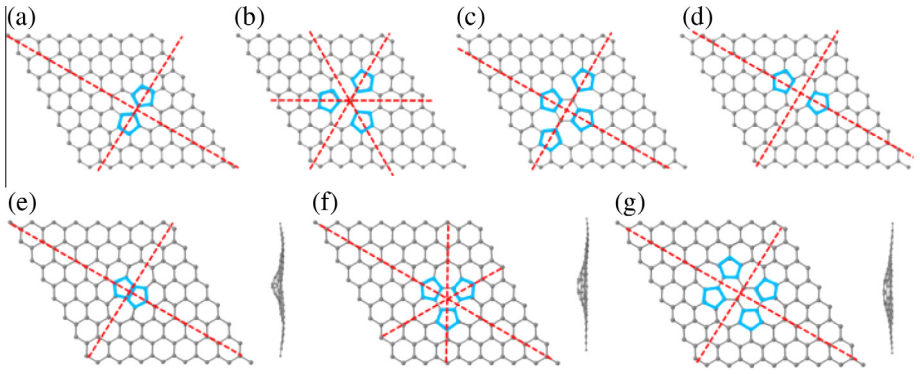

Fig. 1 – Schematic of the investigated topological defect structures: (a) SW, (b) V_2(555-777), (c) V_2(5555-6-7777), (d) V_2(5-8-5), (e) I_2(ISW), (f) I_2(555-6-777), (g) I_2(5555-66-7777). Symmetry lines are shown as red, dashed lines. Five-membered carbon rings are outlined in blue. The SW and V_2 structures (upper panels) remain planar while the I_2 structures (lower panels) contain hillocks that are shown in the side-view snapshots. (A colour version of this figure can be viewed online.)

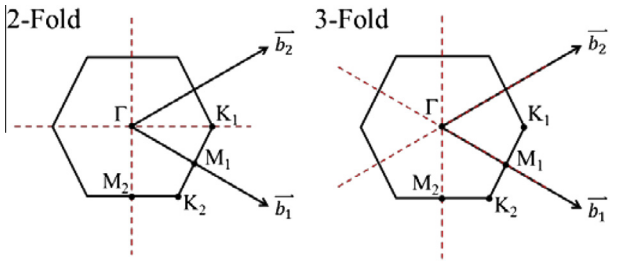

Fig. 2 – Schematic of the Brillouin zones for the listed degree of symmetry. The high symmetry points, symmetry lines, and reciprocal lattice vectors are also shown. (A colour version of this figure can be viewed online.)

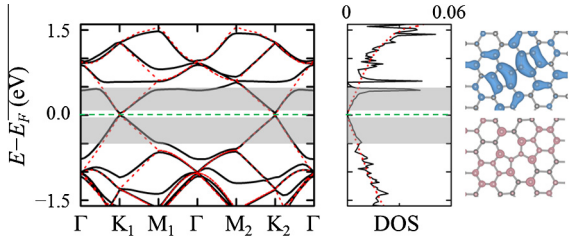

Fig. 3 – Band structure (left) and density of states (DOS in eV^{-1} $Å^{-2}$) (middle) of the Stone-Wales defect (black, solid) and pristine graphene (red, dashed) cases with the Fermi level indicated by the green, dashed line. Band decomposed charge density isosurfaces of the shaded regions are displayed to the right (±0.002 e/bohr^3). (A colour version of this figure can be viewed online.)

by the increased dispersion of the corresponding bands and the broadening of the DOS peaks within 0.5 eV below E_F. The difference in localization tendency amongst the DV configurations is likely related to the relative stability of the coupling of the p_z states in the defect region. In addition, the increased coupling of the quasi-localized p_z states in the V_2(555-777) > V_2(5555-6-7777) > V_2(5-8-5) cases is reflected by the respective decrease in E_f and increase in the shift of E_F from that of graphene [Fig. S1].

The band structures [left] and DOS [middle] for each of the DIs are presented in Fig. 5. Here, the introduction of the C–C dimer creates defect states near E_F, rather than adding two electrons into the π system of graphene and shifting the E_F above the CB. Furthermore, the graphene lattice is distorted and forms so-called hillocks in each of these cases, thereby disrupting the graphene π system. Depending on the defect type, the additional p_z states tend to be partially coupled to the graphene π bands as seen in the I_2(ISW) and I_2(5555-66-7777) cases or highly localized such as in the I_2(555-6-777) case. Comparing the former two cases, we observe that the dispersion of the bands is reduced (or the DOS peaks are sharpened) within 0.6 eV of E_F in the I_2(5555-66-7777) case, suggesting that a greater fraction of p_z states are quasi-localized as a result of the greater extent in lattice disorder. In the I_2(555-6-777) case, the partially filled flat bands (or sharp DOS peaks) at E_F are primarily attributed to the sp^3-like dangling bonds and p_z orbitals of the hillock C atoms. Similarly, such flat bands at E_F have been identified in zigzag graphene nanoribbons (GNR) in large association with the sp^2-like dangling bonds [48]. These results suggest that upon electron (hole) injection, the quasi-localized states in the vicinity of the defect are preferentially filled (emptied).

3.2. *Impact of topological defects on capacitance*

The quantum capacitance of graphene-based electrodes is defined as $C_Q = d\sigma/d\phi_G$, where $d\sigma$ and $d\phi_G$ refer to the variations of charge density and local potential in graphene, respectively, and is given by [23]:

$$C_Q = e^2 \int_{-\infty}^{+\infty} D(E) F_T(E-\mu) dE \quad (1)$$

where $D(E)$ is the DOS, $F_T(E)$ is the thermal broadening function [$=(4kT)^{-1}\mathrm{sech}^2(E/2kT)$], E is the relative energy with respect to E_F, μ is the chemical potential ($=e\phi_G$), and e is the elementary charge.

Fig. 6 shows the calculated C_Q for pristine [(a)] and each of the defective [(b–h)] graphene electrodes at 300 K, which tend to resemble their respective DOS profiles under thermal broadening. In Fig. 6(a), we observe that the C_Q of pristine

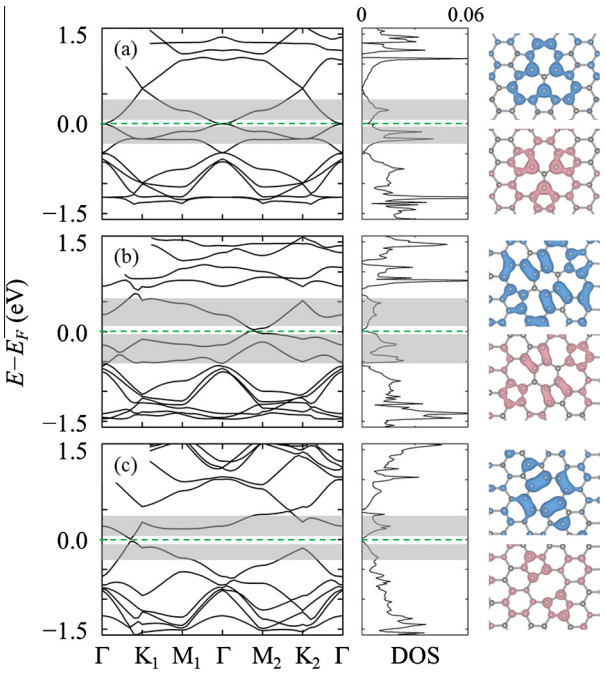

Fig. 4 – Band structure (left) and density of states (DOS in eV^{-1} Å^{-2}) (middle) of the (a) V_2(555-777), (b) V_2(5555-6-7777), and (c) V_2(5-8-5) cases with the Fermi level indicated by the green, dashed line. Band decomposed charge density isosurfaces of the shaded regions are displayed to the right (±0.002 *e*/bohr^3). (A colour version of this figure can be viewed online.)

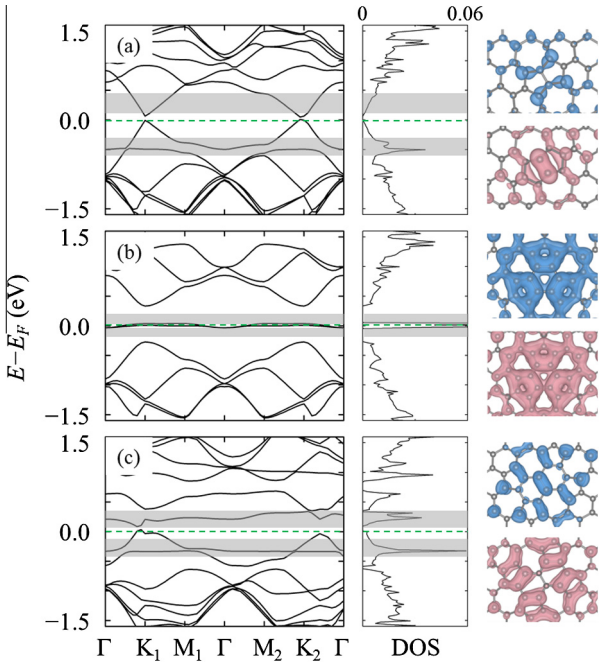

Fig. 5 – Band structure (left) and density of states (DOS in eV^{-1} Å^{-2}) (middle) of the (a) I_2(ISW), (b) I_2(555-6-777), and (c) I_2(5555-66-7777) cases with the Fermi level indicated by the green, dashed line. Band decomposed charge density isosurfaces of the shaded regions are displayed to the right (±0.002 *e*/bohr^3). (A colour version of this figure can be viewed online.)

graphene is zero at $\phi_G = 0$ V where the Dirac cone is located but increases linearly to around 250 F/g at $\phi_G = \pm 1$ V. In contrast, all of the defective graphene sheets tend to have highly irregular C_Q profiles with local sharp enhancements close to the neutrality point; these peaks correspond to the aforementioned quasi-localized p_z states.

In Fig. 7, we show σ as a function of ϕ_G to represent the cumulative excess charge in the electrode at a given electrode potential. The defective graphene electrodes generally store more charge than pristine graphene within the 2 V window presented here, although the V_2(555-777) case is the exception beyond $\phi_G < 0.75$ V. This increased charge capacity is a direct consequence of the additional availability of states near E_F. In other words, to achieve the same electrode charge density, a lower ϕ_G is required for the defective graphene electrodes. However, it is also evident that these electrodes no longer store charge symmetrically. As a result, certain defect types are better suited for different terminals; the SW case, for example, is clearly more effective as a negative electrode while the V_2(555-777), V_2(5555-6-7777), and I_2(ISW) cases are more effective as positive electrodes.

Along with C_Q, the electric double layer (EDL) capacitance (C_D) will also influence the total interfacial capacitance (C_T), which is given by $1/C_T = 1/C_Q + 1/C_D$. The EDL capacitance is evaluated based on the microstructure of the electrolyte near the electrode under applied potential and has been studied using computational methods for a variety of ILs near pristine graphene [23,49–54]. However, the presence of defects affects the charge distribution along the electrode surface, which in turn may influence the IL arrangement near the surface. For example, our previous work [25] with nitrogen-doped graphene at 2.7 at.% showed that the maximum (minimum) atomic charge near the defect sites was 0.66 (−1.14) when $\sigma = 5.43$ μC/cm^2. Yet, the N-doping was found to have little influence on the EDL microstructure and capacitance.

According to Bader charge analysis [Fig. S2], the injection of one electron or hole into the defect lattice with $n_d = 3 \times 10^{13}$ cm^{-2} (≈0.8 at.%) is spread broadly, with a maximum (minimum) atomic charge of 0.20 (−0.25) *e* on select atoms. Given that the charge distribution exhibits smaller fluctuations compared to the N-doped case, we can expect that these small point-like topological defects will also have a marginal effect on C_D (see Fig. S3 in Supporting Information). We should note that in the DI cases, the curvature of the hillocks could additionally affect C_D; previous studies have demonstrated that C_D improves with increasing electrode curvature [55–57] or surface roughness [58,59]. However, we can expect the effect of surface topology on C_D to also be marginal since the hillocks are both isolated and have small curvature. In short, the C_D using graphene electrodes with the considered topological defects is likely similar to that of pristine graphene electrodes, although this may not be the case when we consider larger concentrations of defects or larger-scale defects. We therefore expect C_T to correspondingly increase due to the enhanced C_Q (possible C_D/C_T profiles are shown in Figs. S4 and S5 in Supporting Information), which is similarly demonstrated in the case of N-doping [18,24,25]. To the best of our knowledge, comparisons to experimental results are not possible at this time since the (differential) C_T of supercapacitors using graphene with topological defects has never been reported. But we

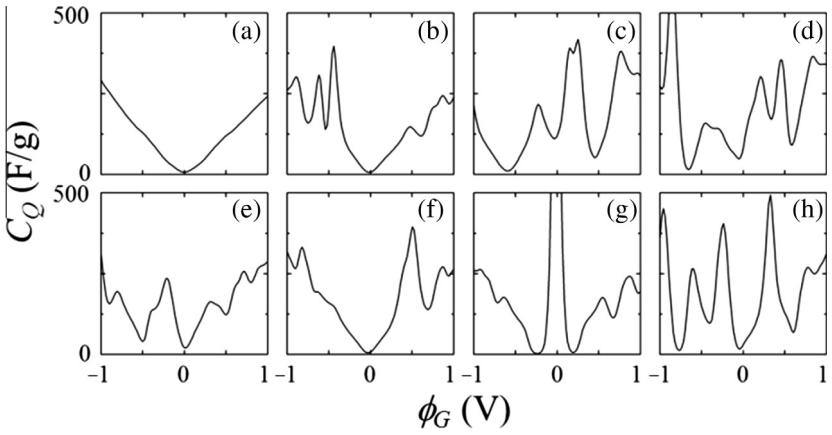

Fig. 6 – Calculated quantum capacitance (C_Q) of the (a) pristine graphene and the (b) SW, (c) V_2(555-777), (d) V_2(5555-6-7777), (e) V_2(5-8-5), (f) I_2(ISW), (g) I_2(555-6-777), and (h) I_2(5555-66-7777) defect cases. All profiles are shown as a function of the local electrode potential (ϕ_G).

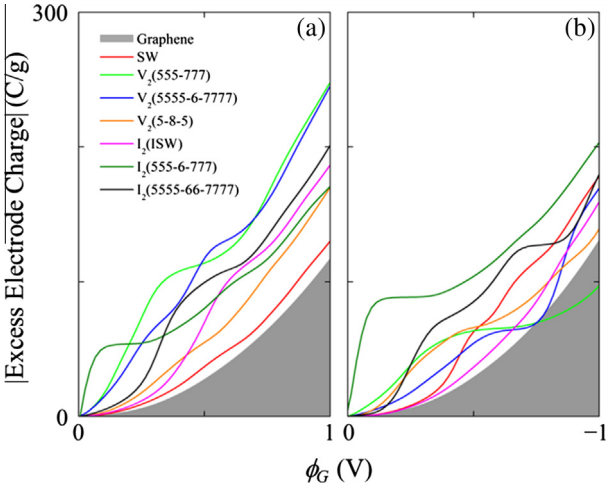

Fig. 7 – Comparison of the total amount of excess charge stored under (a) positive and (b) negative bias for pristine graphene and each defective graphene sheet as a function of the local electrode potential (ϕ_G). (A colour version of this figure can be viewed online.)

should also note that our quantitative results may require further refinement. For instance, we have neglected the possible polarization of the electrodes [53] and IL ions at the interface and its effects on the electrode charge redistribution, the space charge density, and subsequently, C_D. In addition, the DOS (and C_Q) may be altered to a certain extent if the electronic structure is locally modified by electrode–IL interactions, which were omitted for simplicity. Nonetheless, our analysis clearly shows that topological defects can have a profound impact on, and likely improve, C_Q and thus, C_T.

3.3. *Tuning the electronic structure and quantum capacitance using topological defects*

In Section 3.2, we presented the electronic structure and C_Q of individual topological defects. Experimentally, however, it may be quite challenging to recreate such homogeneity along the graphene lattice. Therefore in Section 3.3, we increase the complexity by exploring the impact of having different combinations of topological defects on the electronic structure and C_Q. To this end, we have simulated two scenarios: graphene sheets with an overall $n_d = 3 \times 10^{13}$ cm^{-2} using (1) SW, V_2(555-777), I_2(555-6-777), and I_2(5555-66-7777) defects [Fig. 8(a)] and (2) V_2(555-777) and I_2(5555-66-7777) defects at a 3:1 ratio [Fig. 8(b)].

Fig. 8(a and b) show the DOS of each of the respective configurations of defective graphene sheets, which exhibit several sharp peaks near E_F. According to our analysis of the projected DOS [Fig. S6], each of these peaks is attributed to a particular defect-induced quasi-localized state (see markings), which has been similarly observed in previous theoretical work [46,60]. Note that the positions of these quasi-localized states relative to each other remain largely unchanged; the position of E_F is approximated by the (density-weighed) average positions of each E_F in the associated individual defect cases (which can be possible when long-range coupling between adjacent defect types is absent; see Figs. S7 and S8 for further discussion). This analysis implies that the following two-step process can be used to tailor the electronic structure of defective graphene: (1) determine the relative positions of quasi-localized states from the chosen array of topological defects and (2) shift the position of E_F based on the densities of each topological defect. However, this procedure is likely possible only when defect states are both relatively close in energy and coupled to the π system; without these conditions, gaps in the DOS would appear between the localized states.

Fig. 8(a and b) also depict the predicted C_Q of the mixed defect electrodes at 300 K. We additionally plot σ as a function of ϕ_G in the insets. Similar to the individual defect cases, while σ tends to be larger than that of pristine graphene, the predicted enhancement will vary between the positive and negative terminal. In fact in both cases, a larger σ is favored at the positive electrode. This suggests that graphene electrodes can be individually tailored for operation as either the

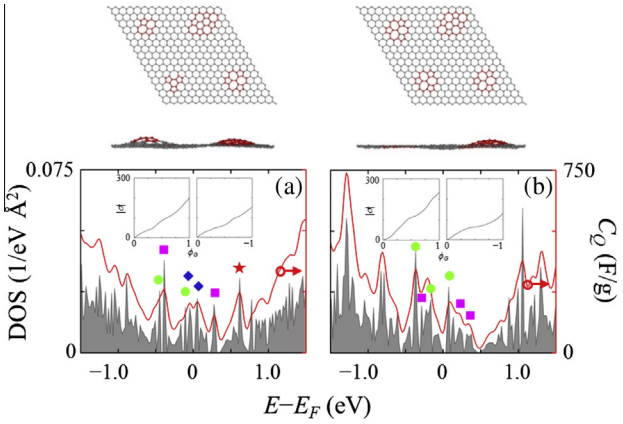

Fig. 8 – The density of states (DOS) and quantum capacitance (C_Q) of the (a) SW/V_2(555-777)/I_2(555-6-777)/I_2(5555-66-7777) and (b) V_2(555-777)/I_2(5555-66-7777) at 3:1 ratio mixed defect cases (the upper panel shows top- and side-view schematics of the corresponding structures with the defect region highlighted in red); the DOS (C_Q) is depicted by the shaded region (red line). The markings indicate the positions of resonant defect states associated with the (★) SW, (●) V_2(555-777), (♦) I_2(555-6-777), and (■) I_2(5555-66-7777) defects. The inset shows the excess electrode charge (|σ| in C/g) as a function of electrode potential (ϕ_G in V). (A colour version of this figure can be viewed online.)

positive or negative electrode; the use of asymmetric electrodes for supercapacitors has the potential to significantly increase performance and deserves further investigation.

4. Conclusion

We have investigated the impact of topological defects on the electronic structure and quantum capacitance of graphene using density functional theory. In this study, we considered small point-like defects such as Stone-Wales, di-vacancies, and di-interstitials. The presence of these defects disrupts the π system of graphene, which gives rise to quasi-localized states of varying degrees near the Fermi level. As a result, each of these defective graphene electrodes tends to have enhanced quantum capacitance compared to pristine graphene, (while the double layer capacitance tends to remain virtually unaffected by the presence of these small SW, V_2, and I_2 defects considered). Interestingly, their charging behavior is found to be asymmetric around the neutrality point such that some defective graphene sheets are more effective as either the positive or negative electrode. Our analysis also suggests that the double layer capacitance remains virtually unaffected by the presence of these defects. These findings indicate that graphene electrodes with topological defects may be used to enhance the overall capacitance of supercapacitors by virtue of the increased quantum capacitance. Furthermore, our study suggests that graphene-based electrodes can be specifically tailored as separate positive and negative electrodes, which could significantly enhance the performance of supercapacitors and warrants further study.

Acknowledgment

This work was supported by the R.A. Welch foundation (F-1535). We would also like to thank the Texas Advanced Computing Center for use of the Stampede supercomputing system (OCI-1134872).

Appendix A. Supplementary data

Supplementary data associated with this article can be found, in the online version, at http://dx.doi.org/10.1016/j.carbon.2013.11.057.

REFERENCES

[1] Conway BE. Electrochemical Supercapacitors: Scientific Fundamentals and Technological Applications. New York NY: Kluwar Academic; 1999.
[2] Wang G, Zhang L, Zhang J. A review of electrode materials for electrochemical supercapacitors. Chem Soc Rev 2012;41(2):797–828.
[3] Simon P, Gogotsi Y. Capacitive energy storage in nanostructured carbon-electrolyte systems. Acc Chem Res 2013;46(5):1094–103.
[4] Zhu Y, Murali S, Stoller MD, Ganesh KJ, Cai W, Ferreira PJ, et al. Carbon-based supercapacitors produced by activation of graphene. Science 2011;332(6037):1537–41.
[5] El-Kady MF, Strong V, Dubin S, Kaner RB. Laser scribing of high-performance and flexible graphene-based electrochemical capacitors. Science 2012;335(6074):1326–30.
[6] Huang X, Qi X, Boey F, Zhang H. Graphene-based composites. Chem Soc Rev 2012;41(2):666–86.
[7] Wang Y, Shi Z, Huang Y, Ma Y, Wang C, Chen M, et al. Supercapacitor devices based on graphene materials. J Phys Chem C 2009;113(30):13103–7.
[8] Chen J, Li C, Shi G. Graphene materials for electrochemical capacitors. J Phys Chem Lett 2013;4(8):1244–53.
[9] Li J, Östling M. Prevention of graphene restacking for performance boost of supercapacitors—a review. Crystals 2013;3(1):163–90.
[10] Le LT, Ervin MH, Qiu H, Fuchs BE, Lee WY. Graphene supercapacitor electrodes fabricated by inkjet printing and thermal reduction of graphene oxide. Electrochem Commun 2011;13(4):355–8.
[11] Liu C, Yu Z, Neff D, Zhamu A, Jang BZ. Graphene-based supercapacitor with an ultrahigh energy density. Nano Lett 2010;10(12):4863–8.
[12] Guo CX, Li CM. A self-assembled hierarchical nanostructure comprising carbon spheres and graphene nanosheets for enhanced supercapacitor performance. Energy Environ Sci 2011;4(11):4504–7.
[13] Yang X, Cheng C, Wang Y, Qiu L, Li D. Liquid-mediated dense integration of graphene materials for compact capacitive energy storage. Science 2013;341(6145):534–7.
[14] Yoo JJ, Balakrishnan K, Huang J, Meunier V, Sumpter BG, Srivastava A, et al. Ultrathin planar graphene supercapacitors. Nano Lett 2011;11(4):1423–7.
[15] Choi BG, Hong J, Hong WH, Hammond PT, Park H. Facilitated ion transport in all-solid-state flexible supercapacitors. ACS Nano 2011;5(9):7205–13.
[16] Jung HY, Karimi MB, Hahm MG, Ajayan PM, Jung YJ. Transparent, flexible supercapacitors from nano-engineered carbon films. Sci Rep 2012;2:773–7.

[17] Qiu Y, Zhang X, Yang S. High performance supercapacitors based on highly conductive nitrogen-doped graphene sheets. Phys Chem Chem Phys 2011;13(27):12554–8.
[18] Jeong HM, Lee JW, Shin WH, Choi YJ, Shin HJ, Kang JK, et al. Nitrogen-doped graphene for high-performance ultracapacitors and the importance of nitrogen-doped sites at basal planes. Nano Lett 2011;11(6):2472–7.
[19] Jiang B, Tian C, Wang L, Sun L, Chen C, Nong X, et al. Highly concentrated, stable nitrogen-doped graphene for supercapacitors: simultaneous doping and reduction. Appl Surf Sci 2012;258(8):3438–43.
[20] Sun L, Wang L, Tian C, Tan T, Xie Y, Shi K, et al. Nitrogen-doped graphene with high nitrogen level via a one-step hydrothermal reaction of graphene oxide with urea for superior capacitive energy storage. RSC Adv 2012;2(10):4498–506.
[21] Xia J, Chen F, Li J, Tao N. Measurement of the quantum capacitance of graphene. Nat Nanotechnol 2009;4(8):505–9.
[22] Stoller MD, Magnuson CW, Zhu Y, Murali S, Suk JW, Piner R, et al. Interfacial capacitance of single layer graphene. Energy Environ Sci 2011;4(11):4685–9.
[23] Paek E, Pak AJ, Hwang GS. A computational study of the interfacial structure and capacitance of graphene in [BMIM][PF6] ionic liquid. J Electrochem Soc 2013;160(1):A1–A10.
[24] Zhang LL, Zhao X, Ji H, Stoller MD, Lai L, Murali S, et al. Nitrogen doping of graphene and its effect on quantum capacitance, and a new insight on the enhanced capacitance of N-doped carbon. Energy Environ Sci 2012;5(11):9618–25.
[25] Paek E, Pak AJ, Kweon KE, Hwang GS. On the origin of the enhanced supercapacitor performance of nitrogen-doped graphene. J Phys Chem C 2013;117(11):5610–6.
[26] Armand M, Endres F, MacFarlane DR, Ohno H, Scrosati B. Ionic-liquid materials for the electrochemical challenges of the future. Nat Mater 2009;8(8):621–9.
[27] Liu H, Liu Y, Li J. Ionic liquids in surface electrochemistry. Phys Chem Chem Phys 2010;12(8):1685–97.
[28] Luryi S. Quantum capacitance devices. Appl Phys Lett 1988;52(6):501–3.
[29] Banhart F, Kotakoski J, Krasheninnikov AV. Structural defects in graphene. ACS Nano 2011;5(1):26–41.
[30] Kotakoski J, Meyer JC, Kurasch S, Santos-Cottin D, Kaiser U, Krasheninnikov AV. Stone-Wales-type transformations in carbon nanostructures driven by electron irradiation. Phys Rev B 2011;83(24):245420.
[31] Kotakoski J, Krasheninnikov AV, Kaiser U, Meyer J. From point defects in graphene to two-dimensional amorphous carbon. Phys Rev Lett 2011;106(10):105505.
[32] Ugeda MM, Brihuega I, Hiebel F, Mallet P, Veuillen J-Y, Gómez-Rodríguez JM, et al. Electronic and structural characterization of divacancies in irradiated graphene. Phys Rev B 2012;85(12):121402.
[33] Perdew JP, Wang Y. Accurate and simple analytic representation of the electron-gas correlation energy. Phys Rev B 1992;45(23):13244–9.
[34] Kresse G, Furthmüller J. Efficient iterative schemes for *ab initio* total-energy calculations using a plane-wave basis set. Phys Rev B 1996;54(16):11169–86.
[35] Blöchl PE. Projector augmented-wave method. Phys Rev B 1994;50(24):17953–79.
[36] Monkhorst HJ, Pack JD. Special points for Brillouin-zone integrations. Phys Rev B 1976;13(12):5188–92.
[37] Henkelman G, Arnaldsson A, Jónsson H. A fast and robust algorithm for Bader decomposition of charge density. Comput Mater Sci 2006;36(3):354–60.
[38] Stone AJ, Wales DJ. Theoretical studies of icosahedral C60 and some related species. Chem Phys Lett 1986;128(5):501–3.
[39] Li L, Reich S, Robertson J. Defect energies of graphite: density-functional calculations. Phys Rev B 2005;72(18):184109.
[40] Ma J, Alfè D, Michaelides A, Wang E. Stone-Wales defects in graphene and other planar sp^2-bonded materials. Phys Rev B 2009;80(3):033407.
[41] El-Barbary AA, Telling RH, Ewels CP, Heggie MI, Briddon PR. Structure and energetics of the vacancy in graphite. Phys Rev B 2003;68(14):144107.
[42] Zhang H, Zhao M, Yang X, Xia H, Liu X, Xia Y. Diffusion and coalescence of vacancies and interstitials in graphite: a first principles study. Diamond Relat Mater 2010;19(10):1240–4.
[43] Lusk MT, Wu DT, Carr LD. Graphene nanoengineering and the inverse Stone-Thrower-Wales defect. Phys Rev B 2010;81(15):155444.
[44] Ma Y. Simulation of interstitial diffusion in graphite. Phys Rev B 2007;76(7):075419.
[45] Lehtinen P, Foster AS, Ayuela A, Krasheninnikov A, Nordlund K, Nieminen RM. Magnetic properties and diffusion of adatoms on a graphene sheet. Phys Rev Lett 2003;91(1):017202.
[46] Lherbier A, Dubois SM-M, Declerck X, Niquet Y-M, Roche S, Charlier J-C. Transport properties of graphene containing structural defects. Phys Rev B 2012;86(7):075402.
[47] Shirodkar SN, Waghmare UV. Electronic and vibrational signatures of Stone-Wales defects in graphene: first-principles analysis. Phys Rev B 2012;86(16):165401.
[48] Castro Neto AH, Guinea F, Peres NMR, Novoselov KS, Geim AK. The electronic properties of graphene. Rev Mod Phys 2009;81(1):109–62.
[49] Vatamanu J, Borodin O, Smith GD. Molecular simulations of the electric double layer structure, differential capacitance, and charging kinetics for N-methyl-N-propylpyrrolidinium bis(fluorosulfonyl)imide at graphite electrodes. J Phys Chem B 2011;115(12):3073–84.
[50] Feng G, Zhang JS, Qiao R. Microstructure and capacitance of the electrical double layers at the interface of ionic liquids and planar electrodes. J Phys Chem C 2009;113(11):4549–59.
[51] Kislenko SA, Samoylov IS, Amirov RH. Molecular dynamics simulation of the electrochemical interface between a graphite surface and the ionic liquid [BMIM][PF6]. Phys Chem Chem Phys 2009;11(27):5584–90.
[52] Vatamanu J, Borodin O, Smith GD. Molecular insights into the potential and temperature dependences of the differential capacitance of a room-temperature ionic liquid at graphite electrodes. J Am Chem Soc 2010;132(42):14825–33.
[53] Merlet C, Péan C, Rotenberg B, Madden PA, Simon P, Salanne M. Simulating supercapacitors: can we model electrodes as constant charge surfaces? J Phys Chem Lett 2013;4(2):264–8.
[54] Wang S, Li S, Cao Z, Yan T. Molecular dynamic simulations of ionic liquids at graphite surface. J Phys Chem C 2010;114(2):990–5.
[55] Feng G, Jiang D, Cummings PT. Curvature effect on the capacitance of electric double layers at ionic liquid/onion-like carbon interfaces. J Chem Theory Comput 2012;8(3):1058–63.
[56] Feng G, Qiao R, Huang J, Dai S, Sumpter BG, Meunier V. The importance of ion size and electrode curvature on electrical double layers in ionic liquids. Phys Chem Chem Phys 2011;13(3):1152–61.
[57] Feng G, Li S, Atchison JS, Presser V, Cummings PT. Molecular insights into carbon nanotube supercapacitors: capacitance independent of voltage and temperature. J Phys Chem C 2013;117(18):9178–86.
[58] Vatamanu J, Borodin O, Bedrov D, Smith GD. Molecular dynamics simulation study of the interfacial structure and differential capacitance of alkylimidazolium

bis(trifluoromethanesulfonyl)imide [$C_n$mim][TFSI] ionic liquids at graphite electrodes. J Phys Chem C 2012;116(14):7940–51.

[59] Xing L, Vatamanu J, Smith GD, Bedrov D. Nanopatterning of electrode surfaces as a potential route to improve the energy density of electric double-layer capacitors: insight from molecular simulations. J Phys Chem Lett 2012;3(9):1124–9.

[60] Cockayne E, Rutter GM, Guisinger NP, Crain JN, First PN, Stroscio JA. Grain boundary loops in graphene. Phys Rev B 2011;83(19):195425.